Ultramicroscopy 167 (2016) 5–10

Contents lists available at ScienceDirect

Ultramicroscopy

journal homepage: www.elsevier.com/locate/ultramic

Measuring bandgap states in individual non-stoichiometric oxide nanoparticles using monochromated STEM EELS: The Praseodymium–ceria case ☆

W.J. Bowman [a], K. March [b], C.A. Hernandez [a], P.A. Crozier [a,*]

[a] School for the Engineering of Matter, Transport and Energy, Arizona State University, 501 E. Tyler Mall, Tempe, AZ 85287-6106, United States
[b] Laboratoire de Physique des Solides, Université Paris-Sud, CNRS, UMR 8502, 91405 Orsay Cedex, France

A R T I C L E I N F O

Article history:
Received 22 December 2015
Received in revised form
21 April 2016
Accepted 26 April 2016
Available online 27 April 2016

Keywords:
Monochromated scanning transmission electron microscopy (STEM)
Electron energy-loss spectroscopy (EELS)
Inter-band states
Single scattering distribution
Cerium dioxide (CeO_2)

A B S T R A C T

We describe a method to perform high spatial resolution measurement of the position and density of inter-band impurity states in non-stoichiometric oxides using ultra-high energy resolution electron energy-loss spectroscopy (EELS). This can be employed to study optical and electronic properties of atomic and nanoscale defects in electrically-conducting and optically-active oxides. We employ a monochromated scanning transmission electron microscope with subnanometer diameter electron probe, making this technique suitable for correlating spectroscopic information with high spatial resolution images from small objects such as nanoparticles, surfaces or interfaces. The specific experimental approach outlined here provides direct measurement of the Pr inter-band impurity states in $Pr_{0.1}Ce_{0.9}O_{2-\delta}$ via valence-loss EELS, which is interpreted with valence-loss spectral simulation based on density of states data to determine the energy level and character of the inter-band state. Additionally, observation of optical color change upon chemically-induced oxygen non-stoichiometry indicates that the population of the inter-band state is accompanied by an energy level shift within the bandgap.

1. Introduction

Describing how variations in nanoscale structure and composition affect local electronic and optical properties is critical to developing a fundamental understanding of atomic, nanoscale and mesoscale properties of condensed matter [1]. Experimental methods to explore these relationships require a correlative approach to atomic resolution imaging and spectroscopy, and high spatial resolution should allow electronic states associated with nanoparticles and defects such as dislocations or grain boundaries to be mapped and correlated with defect atomic structure [2,3]. For insulators, defects often give rise to states within the bandgap which may often control charge transport properties as well as optical properties. Correlating these states with local structure and composition is the key to understanding and controlling the material properties. Recent developments in monochromated electron energy-loss spectroscopy (EELS) in the aberration-corrected scanning transmission electron microscope (AC-STEM) offer new opportunities for local nanoscale probing of bandgap states, and correlation with structure and chemistry at the 0.1 nm level. The ability to now correlate atomic structure with loss features down to a hundred meV in the energy-loss spectrum represents a powerful tool for characterizing electronic and optical properties of materials—especially semiconductors and insulators, with defects such as surfaces, grain boundaries and interfaces. Here we quantify the energy, width and relative intensity of the density of states within the band gap that are created when solute Pr ions are added to CeO_2 nanoparticles.

The $Pr_xCe_{1-x}O_{2-\delta}$ (PCO) system exhibits mixed ionic-electronic conduction at intermediate temperatures making it attractive in applications demanding counter diffusion of electrons and oxygen ions, such as solid oxide fuel cell electrodes and membranes [4]. We employ a monochromated AC-STEM which combines subnanometer electron probe diameter and EELS with ultra-high energy resolution of 15 meV [5]. The high energy resolution together with an improved modulation transfer function greatly enhances the detection limits for states within the bandgap which have often been obscured by the intense tails on the zero-loss peak (ZLP) in EELS. Here, EELS allows the width and energy position of the state to be determined with respect to the top of the valence band, while optical observations of chemically-induced color changes are employed to provide further information on the

☆Dedicated to Annie and Kato.
* Corresponding author.
E-mail address: crozier@asu.edu (P.A. Crozier).

http://dx.doi.org/10.1016/j.ultramic.2016.04.009
0304-3991/

energy shift of the inter-band state when the Pr oxidation state is changed.

Ceria (CeO_2) is an insulating oxide which forms mobile oxygen vacancies under strongly reducing conditions or at elevated temperatures, and accommodates the addition of aliovalent cations to form oxygen-deficient solid solutions with wide-ranging electrical, optical and catalytic properties [6,7]. For example, the ability to enhance redox activity or oxygen ionic conductivity by adding fixed-valence metal cations such as Y^{3+}, Ca^{2+}, Sm^{3+} or Gd^{3+} has made these mixed oxides attractive options for device applications such as oxygen permeation membranes, gas sensors and solid oxide fuel cells [8–10]. The situation is rather more interesting when the added cation is—like Ce, multivalent. For example, in the PCO system an impurity band below the conduction band of ceria is formed under mildly reducing conditions when electron density is localized on a Pr^{3+} ion (the result of oxygen release) and may transfer, or hop, to an adjacent Pr^{4+} ion [11,12]. The probability of this polaron hopping mechanism is influenced by the spatial separation of adjacent +3 and +4 Pr ions; it is thus sensitive to Pr concentration and oxidation state—which can be modulated via temperature and ambient. In fact, experimental evidence indicates that impurity band formation occurs primarily when $x > 0.1$ in $Pr_xCe_{1-x}O_{2-\delta}$ [13].

We recently reported a substantial enhancement in the electrical conductivity of grain boundaries in $Gd_xCe_{1-x}O_{2-\delta}$ upon Pr^{4+} addition (i.e. $Gd_xPr_yCe_{1-x-y}O_{2-\delta}$), which was accompanied by a factor of three enrichment in the Pr concentration at grain boundary cores [14]. It was speculated that electronic conductivity via Pr^{3+} polaron hopping at Pr-enriched grain boundaries was the origin of the measured conductivity enhancement; however, spectroscopic evidence was not provided for the existence of a Pr impurity conduction band. Here we show that the Pr impurity band can be detected in nanoparticles of $Pr_{0.1}Ce_{0.9}O_{2-\delta}$ using ultra-high energy resolution EELS. The occupancy of the band is determined by the oxidation state of the Pr which can also be determined with EELS. The ability to probe inter-band electronic defect states with nanometer spatial resolution will enable direct interpretation of the relationship between atomic structure and electronic transport or optical properties of defects such as dislocation cores and grain boundaries.

2. Results and discussion

2.1. EELS measurement

PCO nanoparticles approximately 30 nm in diameter, shown in Fig. 1a, were synthesized via spray drying [15]. The as-synthesized particles were initially non-stoichiometric and thus heated under air at 900 °C for 3 h to achieve full oxygen stoichiometry before EELS analysis using a Nion UltraSTEM100 STEM operating at 60 kV accelerating voltage. Valence-loss EELS data were acquired under monochromated condition using a dispersion of 3 meV/channel. Under this condition, the zero-loss elastic peak (instrument response function; ZLP) full width half maximum (FWHM) was typically 18 meV to provide reasonable signal-to-noise; the beam current at the specimen was approximately 1 pA. The convergence and collection angles were 30 mrad and 50 mrad, respectively. Eight valence-loss spectra were acquired from particles and particle clusters in random orientations. The spectra were similar suggesting that orientational effects were not prominent in part because of the large convergence and collection angles employed.

A typical annular dark-field image obtained with the monochromated probe is shown in Fig. 1b. It is possible to achieve a probe diameter of 0.3 nm with the monochromator slit adjusted to give 20 meV spectral resolution; however, to achieve higher beam current the probe size was slightly larger than 0.7 nm for the conditions employed here. The high spatial resolution allows the spectra to be correlated with sub-nanometer features in the sample. However the spatial resolution of the energy loss spectra is determined not by the probe size, but by delocalization effects as predicted by dielectric theory, which are likely to be 5 nm or more in this case. Spectra were recorded in both transmission and aloof beam mode (with the beam positioned a few nanometers outside of the particles). No significant difference was observed in the shape of the intensity within the bandgap region, suggesting that radiation damage effects were minimal. The spectra shown here were recorded in transmission mode.

Core-loss EELS data were acquired from Ce M_{45} and Pr M_{45} edges using a dispersion of 100 meV/channel under non-monochromated condition, under which the ZLP FWHM was approximately 250 meV—the energy spread of the instrument's cold field-emission gun.

Valence-loss EELS of PCO, shown in Fig. 2a, revealed an inter-band feature with rising onset and extended plateau ahead of the

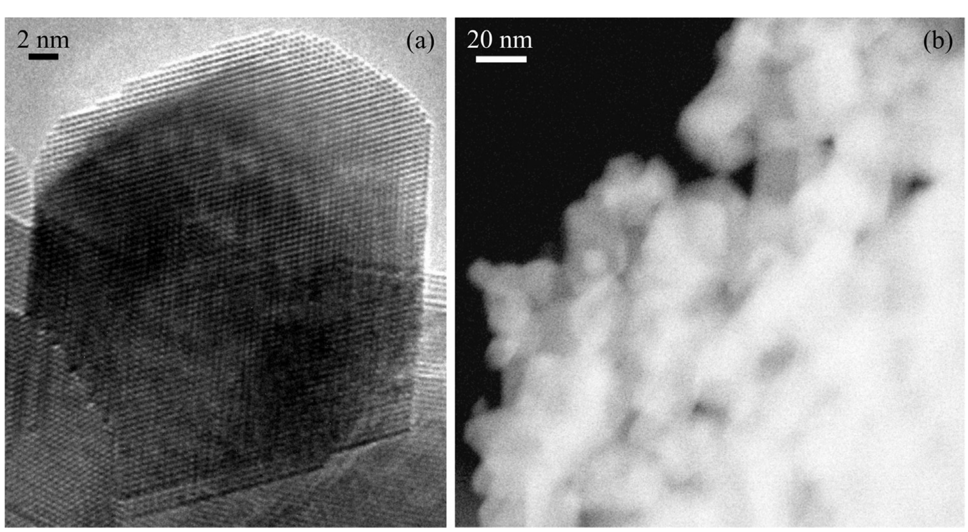

Fig. 1. (a) HRTEM image of typical PCO particle acquired using JEOL 2010 F. (b) Monochromated ADF STEM image of PCO particle cluster.

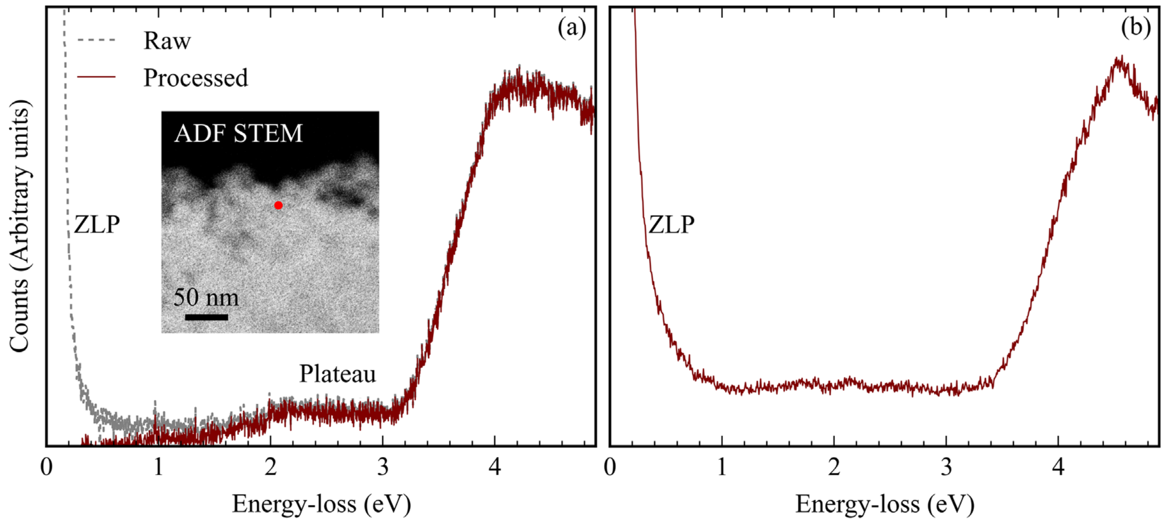

Fig. 2. (a) Typical valence-loss spectra from (a) oxidized PCO—showing ZLP, inter-band plateau feature and conduction band onset, and (b) fragment of bulk CeO_2. The beam position during PCO spectra acquisition is indicated in the monochromated ADF STEM image inset in (a).

conduction band onset. An inverse power law function was fit to the ZLP tail such that the background intensity was approximately zero ahead of the plateau onset. The Cherenkov condition for 60 kV electrons (i.e. refractive index of medium, n, must exceed 2.3) propagating through PCO is unlikely to be satisfied (refractive indices for lanthanide-CeO_2 solid solutions ($La_{0.15}Ce_{0.85}O_{2-\delta}$, La = lanthanide ion) range from 1.65 to 1.95 [16]). Typical reported values of n for pure CeO_2 (about 1.8–2.5 for photon energies below approximately 2.7 eV [17,18–23]) are in some cases sufficiently great to satisfy the Cherenkov condition. However for the PCO particles, radiation would likely be suppressed as the 30 nm particle diameter in this work is significantly less than the emitted photon wavelength [24–26]. Thus no correction for Cherenkov effects was performed during background removal. For reference, valence-loss spectra were acquired from fragments of a crushed bulk CeO_2 solid sample. These data, shown in Fig. 2b, revealed constant intensity within the gap attributed to Cherenkov radiation. The Cherenkov intensity is higher in this specimen in part due to the relatively thicker (greater than several hundred nanometers) fragments that were analyzed. There is no evidence for a significant plateau in the bandgap region from pure CeO_2.

The PCO conduction band onset was measured to be 3.2 ± 0.1 eV (error is one standard deviation)—taken as the intercept of the energy axis with the linear extrapolation of the conduction band onset, and is consistent with that of our reference CeO_2 (3.2–3.4 eV), and literature (3.0–3.2 eV [21,29]). The valence-to-conduction band excitation in CeO_2 is attributed to transitions from occupied levels at the O 2*p* valence band maximum into unoccupied Ce 4*f* states at the conduction band minimum, which are dipole-allowed due to strong covalent hybridization between occupied O 2*p* states and Ce 4*f* states, and unoccupied O 2*p* states and 5*d* states in CeO_2 [27–30]. The pre-plateau rise spanned the energy range of approximately 1.4–2.4 eV with the plateau extending from 2.4 eV to the conduction band edge. The inter-band feature was attributed to a Pr impurity band, facilitating electronic transitions from the O 2*p* valence band into unoccupied Pr 4*f* levels lying below the Ce 4*f* levels of the CeO_2 conduction band [12,13], stemming presumably from hybridization between O 2*p* and Pr 4*f* levels. The plateau onset energy, 1.4 ± 0.3 eV, was taken to be the position of the Pr impurity band.

To verify that the inter-band intensity in the valence-loss spectrum was unambiguously associated with the tetravalent Pr impurity band, we examined Ce/Pr M_{45} edge core-loss spectra in an attempt to detect core-level excitations into unoccupied Pr 4*f* levels associated with Pr^{4+} ions. The M_{45} multiplet structure (*white lines*) in core-loss spectroscopy of lanthanides results from transitions from 3*d* initial states into unoccupied 4*f* orbitals according to $3d^{10}4f^{\,n} \rightarrow 3d^9 4f^{\,n+1}$, with the relative multiplet intensities and spectral fine structure present in each multiplet indicative of cation valence [31,32]. Thus, the separation between the Ce and Pr M_5 white lines was monitored under various acquisition conditions to verify that Pr^{4+} ions were present in the specimen. This approach was employed successfully by López-Cartes et al., who demonstrated that during sequential heating of $Pr_{0.2}Ce_{0.8}O_{2-\delta}$ under gaseous H_2, the reduction of Pr^{4+} to Pr^{3+} was initiated at a significantly lower temperature than was the reduction of Ce^{4+}, and was accompanied by a 1.4 eV contraction in the separation between Ce and Pr M_5 EELS white lines relative to the initial Ce^{4+}/Pr^{4+} separation [33]. This result was later corroborated by precise defect analysis of $Pr_{0.1}Ce_{0.9}O_{2-\delta}$ by Bishop et al. who employed DC conductivity measurements and thermogravimetric analysis to show that the Pr redox couple is active under significantly less reducing conditions than that of Ce [11].

The Ce and Pr M_{45} multiplet structures are well-characterized under +3 and +4 valence conditions, and it is thus straightforward to identify spectral components attributable to both tri- and tetra-valent cations from comparison with published electron energy-loss [28,33,34] and X-ray absorption spectra [30,32,35–37].

As a first step to detecting tetravalent Pr in the specimen, Ce and Pr M_{45} core-loss spectra, shown in Fig. 3, were acquired serially with a static electron probe to ensure reduction of Pr^{4+} to Pr^{3+} via electron beam-induced ionization. A representative spectrum is presented in Fig. 3 (*Reduced*), clearly resolving a low-energy shoulder on the Pr M_4 edge at about 950 eV consistent with trivalent Pr [36]. Simultaneously the Ce M_{45} edge exhibits features consistent with mixed +4/+3 valence: The most intense peaks in each multiplet, as well as associated satellite peaks (approximately 5 eV greater in energy) are the primary white line features for Ce^{4+} [32]; whereas the clearly resolved lower-energy side peaks on the Ce white lines are the primary features of the Ce^{3+} white lines [36]. From this spectrum the M_5 peak separation between Ce^{4+} and Pr^{3+} was measured as 46.2 ± 0.1 eV (from each centroid's most intense channel; cited error is one channel (i.e. the dispersion)). Thus, detection of the Pr M_5 white line at greater than 46.2 eV above the Ce^{4+} peak would confirm the presence of Pr^{4+}. Fig. 3 shows a spectrum (*Oxidized*) recorded with lower electron dose wherein only Ce^{4+} was present. Despite relatively poor signal-to-noise, the Pr M_5 edge centroid position was readily

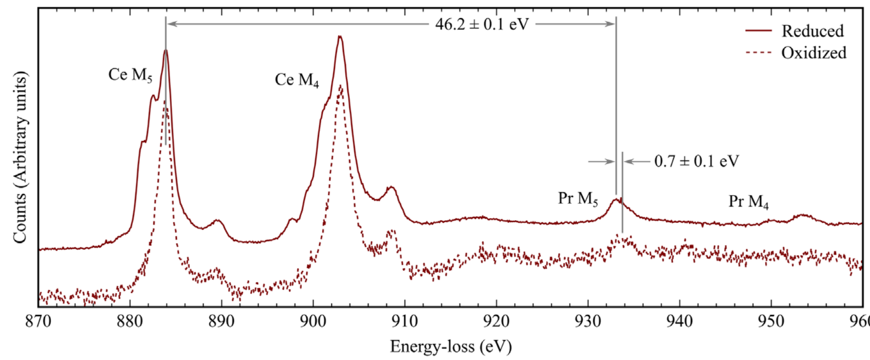

Fig. 3. (*Reduced*) Sum of 30 Ce/Pr M45 core-loss spectra (5 s acquisition) showing mixed-valence Ce and trivalent Pr. (*Oxidized*) Single spectrum (10 s acquisition) showing Ce^{4+} and Pr^{y+}, with $4 > y \geq 3$. The 0.7 eV Pr M_5 edge shift verified the presence of Pr^{4+}.

accessible for measurement in 11 spectra, and it was thus concluded that Pr was predominantly tetravalent in the specimen.

2.2. Spectral modeling

With confidence that the inter-band plateau was associated with the tetravalent Pr impurity band, the experimental valence-loss spectrum (Fig. 2) was characterized following the joint density-of-states (DOS) approximation for the EELS single scattering distribution described by Egerton [38]. This assumes that the variations in spectral intensity over a small range of energy-loss are associated with variations in the valence and conduction band DOS. This was employed to determine the location and width of the unoccupied Pr 4*f* inter-band state. The single scattering intensity, $J^1(E)$, a function of energy loss, E, which is related to a solid's band structure via the joint DOS, $N(E)$, according to Eq. (1). $N(E)$ is the convolution of the initial (occupied) projected DOS in the valence band, $\rho_{VB}(E)$, with the final (unoccupied) projected DOS above the Fermi level in the conduction band, $\rho_{CB}(E)$, i.e.

$$J^1(E) \propto N(E) \propto \rho_{VB}(E) * \rho_{CB}(E) \quad (1)$$

For EELS collection angles employed here, the convolution is dominated by contributions that follow the dipole selection rule between initial and final states. The single scattering distribution approximates the intensity variation around the bandgap region of the EELS spectrum because particles analyzed were thinner than the electron inelastic mean free path for a 60 kV electron in CeO_2 of $\sim$50 nm [39]. Furthermore, the valence-to-conduction band excitations responsible for the conduction band onset in the energy-loss spectrum are not significantly affected by plural scattering. We assumed electronic transitions into the unoccupied Pr 4*f* level were dipole-allowed in the same manner as transitions into Ce 4*f* final states.

Fig. 4a shows symmetry-projected DOS for CeO_2 (calculated in [40]) adapted by shifting the unoccupied DOS to higher energy to match the band gap measurement described in Fig. 2. To model the PCO single-scattering distribution, an unoccupied inter-band Pr 4*f* state was included. This inter-band state was Gaussian, with centroid position and width (at FWHM) varied until principal features in the single-scattering distribution matched the experimental spectrum. In particular, the inter-band plateau onset energy, plateau width, conduction band onset energy and slope were used as optimization parameters. Fig. 4b presents the convolution of the projected DOS in Fig. 4a, and illustrates that electronic transitions from occupied *p*- and *d*-type valence band levels into the unoccupied Pr 4*f* impurity band produce an inter-band plateau. The single-scattering distribution is the sum of the convolved projected DOS, convolved again with a 25 meV (FWHM) Gaussian

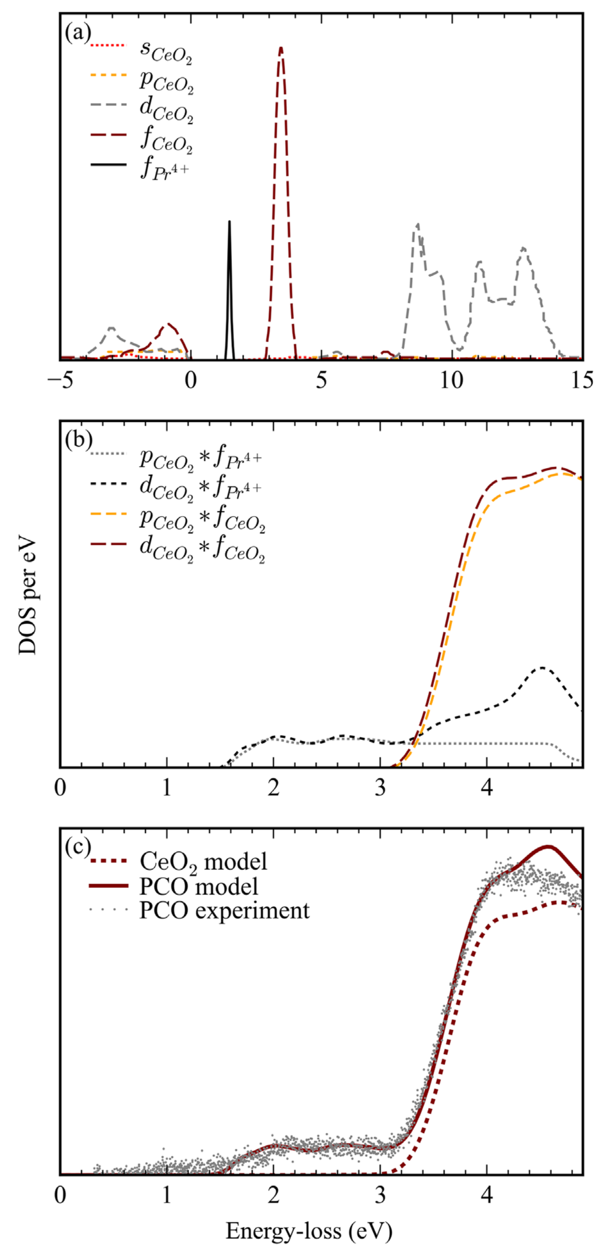

Fig. 4. (a) Symmetry-projected DOS for CeO_2 (adapted from [40]) with unoccupied states shifted to match experimental bandgap measurement, and additional unoccupied Pr 4*f* inter-band state. (0 eV represents the valence band maximum.) (b) Convolution of projected DOS. (c) Single-scattering distributions calculated of model CeO_2 and PCO with overlaid PCO EELS.

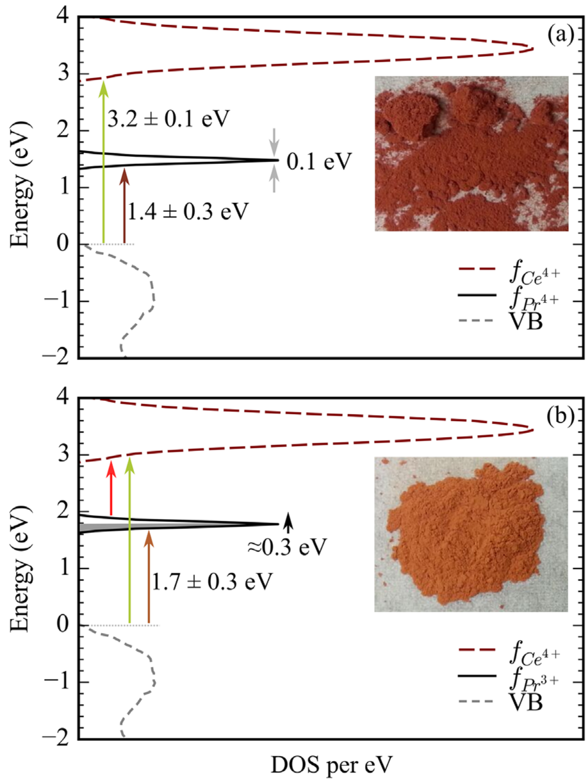

Fig. 5. (a) DOS of oxidized PCO showing valence-to-conduction and valence-to-impurity transitions (labeled arrows). Inset is an image of PCO following heating in air, whereby particles are assumed stoichiometric, with Pr 4*f* impurity band unoccupied (both Ce and Pr are tetravalent). The valence band (VB) is the sum of occupied symmetry-projected DOS (Fig. 4a). (b) Analogous to (a) for reduced PCO wherein Ce is +4 and Pr is a mix of Pr^{4+} and Pr^{3+}. Transitions from Pr impurity into Ce conduction band are optically forbidden (red arrow) *f*–*f* transitions [11]. Inset image of reduced PCO particles following heating in H_2. An approximately +0.3 eV shift (black arrow) is assumed from the observed color change upon Pr^{4+} reduction. (For interpretation of the references to color in this figure legend, the reader is referred to the web version of this article.)

broadening function representing the instrument response function.

The simulated spectra for CeO_2 and PCO are plotted with the experimental PCO spectrum in Fig. 4c. The model CeO_2 distribution lacks the inter-band plateau, instead exhibiting a sharp intensity increase at approximately 3.2 eV, corresponding to the conduction band onset energy of CeO_2 [20,21,29]. (In this approach we ignore excitonic interactions, but Fig. 4 suggests they are not a large effect for this case.) The model PCO distribution tracks the plateau and conduction band onset in the experimental PCO EELS data closely, showing that the Pr impurity DOS is a sharp Gaussian function with energy approximately 1.4 eV above the top of the valence band edge, and approximate width of 0.1 eV at (FWHM). Furthermore, the ratio of integrated Pr and Ce 4*f* DOS, (Pr 4*f*/Ce 4*f*)^{DOS}, is 0.10—approximately the solid's nominal cation composition ratio, C_{Pr}/C_{Ce}=0.11, suggesting that the spectral intensity of the inter-band state varies linearly with Pr concentration. A summary of the experimentally determined PCO electronic structure and model fitting parameters is given in Fig. 5.

Changes in the optical properties of PCO with oxidation state changes are also shown in Fig. 5. As shown in the inset of Fig. 5a, stoichiometric PCO with the Pr 4*f* impurity band unoccupied results in a deep red solid due to absorption via optical excitation into the Pr impurity band. The color is consistent with transition from the valence band into the Pr^{4+} state determined by EELS (energy difference 1.4 ± 0.3 eV as seen in Fig. 5). Immediately following reduction under flowing H_2, the PCO nanoparticles appear orange in color due to the presence of Pr^{3+}, which results from charge transfer resulting from oxygen vacancy formation. This yields a partially filled Pr 4*f* impurity level (shown partially shaded), and color change implying an increase of approximately 0.3 eV in the energy of the Pr 4*f* state. The energy increase results from the increase nuclear screening of the 4*f* level due to the additional electron density associated with the Pr^{3+} cation. (Direct EELS measurements were not performed on the reduced sample because it re-oxidized rapidly following exposure to atmosphere at room temperature). Our analysis is consistent with reports of the PCO optical band gap derived from optical transmission measurements and defect analysis [11–13].

3. Conclusion

In summary, high spatial and energy resolution monochromated EELS has been employed to detect a state within the bandgap of ~30 nm nanoparticles of PCO. Quantitative analysis of the spectra showed that the inter-band state is associated with Pr^{4+} 4*f* levels, has a width of about 0.1 eV, and is located 1.4 eV above the top of the valence band. The strength of the Pr 4*f* DOS relative to the Ce 4*f* DOS scales with the Pr/Ce concentration and is about 0.1. Population and de-population of this state gives rise to color changes in the material attributed to an energy level shift of the impurity state upon population of about +0.3 eV. The ultra-high energy resolution STEM EELS allows inter-band states to be probed with high spatial resolution and should be applicable to other systems where nanocharacterization is required such as grain boundaries, dislocations and precipitates.

Acknowledgments

W.J.B. would like to acknowledge the NSF's Graduate Research Fellowship (DGE-1211230) for continued financial support. P.A.C. and W.J.B. gratefully acknowledge support of NSF Grant DMR-1308085 and access to ASU's John M. Cowley Center for High Resolution Electron Microscopy.

References

[1] L. Sun, D. Marrocchelli, B. Yildiz, Nat. Commun. 6 (2014) 6294.
[2] P.E. Batson, K.L. Kavanagh, J.M. Woodall, J.W. Meyer, Phys. Rev. Lett. 57 (21) (1986) 2729.
[3] S. Lazar, G.A. Botton, M.-Y. Wu, F.D. Tichelaar, H.W. Zandbergen, Ultramic 96 (2003) 535.
[4] H.L. Tuller, S.R. Bishop, Annu. Rev. Mater. Res. 41 (2011) 369.
[5] O.L. Krivanek, T.C. Lovejoy, N. Delby, T. Aoki, R.W. Carpenter, P. Rez, E. Soignard, J. Zhu, P.E. Batson, M.J. Lagos, R.F. Egerton, P.A. Crozier, Nature 514 (2014) 209.
[6] A. Trovarelli, Catalysis by Ceria and Related Materials, 1st ed., Imperial College Press, London, 2002.
[7] H.L. Tuller, A.S. Nowick, J. Electroceram. Soc. 126 (1979) 209.
[8] H.L. Tuller, A.S. Nowick, J. Electroceram. Soc. 122 (1975) 255.
[9] W. Lai, S.M. Haile, J. Am. Ceram. Soc. 88 (2005) 2979.
[10] H.-J. Avila-Paredes, K. Choi, C.-T. Chen, S. Kim. vol. 19, 2009, p. 4837.
[11] S.R. Bishop, T.S. Stefanik, H.L. Tuller, Phys. Chem. Chem. Phys. 13 (2011) 10165.
[12] J.J. Kim, S.R. Bishop, N.J. Thompson, D. Chen, H.L. Tuller, Chem. Mater. 26 (2014) 1374.
[13] J.J. Kim, S.R. Bishop, N. Thompson, Y. Kuru, H.L. Tuller, Solid State Ion. 225 (2012) 198.
[14] W.J. Bowman, J. Zhu, R. Sharma, P.A. Crozier, Solid State Ion. 272 (2015) 9.
[15] V. Sharma, K.M. Eberhardt, R. Sharma, J.B. Adams, P.A. Crozier, Chem. Phys. Lett. 495 (2010) 280.
[16] A. Hartridge, M.G. Krishna, A.K. Bhattacharya, J. Phys. Chem. Solids 59 (1998) 859.
[17] P. Patsalas, S. Logothetidis, C. Metaxa, App. Phys. Lett. 81 (2002) 466.
[18] C. Mansilla, Solid State Sci. 11 (2009) 1456.
[19] N. Özer, Sol. Energy Mater. Sol. Cells 68 (2001) 391.
[20] R.M. Bueno, J.M. Martinez-Duart, M. Hernández-Vélez, L. Vázquez, J. Mater. Sci. 32 (1997) 1861.

[21] F. Goubin, X. Rochquefelte, M.-H. Whangbo, Y. Montardi, R. Brec, S. Jobic, Chem. Mater. 16 (2004) 662.
[22] G. Hass, J.B. Ramsey, R. Thun, J. Opt. Soc. Am. 48 (1958) 324.
[23] T. Wiktorczyk, P. Biegański, E. Zielony, Opt. Mat. 34 (2012) 2101.
[24] A. Rivacoba, N. Zabala, J. Aizpurua, Prog. Surf. Sci. **65** (2000) 1.
[25] M. Stöger-Pollach, H. Franco, P. Schattschneider, S. Lazar, B. Schaffer, W. Grogger, H.W. Zandbergen, Micron 37 (2006) 396.
[26] R. Erni, N.D. Browning, Ultramicroscopy 108 (2008) 84.
[27] E. Wuilloud, B. Delley, W.-D. Scheider, Y. Baer, Phys. Rev. Lett. 53 (1984) 202.
[28] G. Niu, M.A. Schubert, F. d'Acapito, M.H. Zoellner, T. Schroeder, F. Boscherini, J. Appl. Phys. 116 (2014) 123515.
[29] F. Marabelli, P. Wachter, Phys. Rev. B 36 (1987) 1238.
[30] D.R. Mullins, S.H. Overbury, D.R. Huntley, Surf. Sci. 409 (1998) 307.
[31] T. Manoubi, C. Colliex, P. Rez, J. Electron Spectrosc. Relat. Phenom. 50 (1990) 1.
[32] G. Kalkowski, G. Kaindl, G. Wortmann, D. Lentz, S. Krause, Phys. Rev. B 37 (1988) 1376.
[33] C. López-Cartes, S. Bernal, J.J. Calvino, M.A. Cauqui, G. Blanco, J.A. Pérez-Omil, J. M. Pintado, S. Helvig, P.L. Hansen, Chem. Commun. 644 (2003).
[34] S. Turner, S. Lazar, B. Freitag, R. Egoavil, J. Verbeeck, S. Put, Y. Strauven, G. Van Tendeloo, Nanoscale 3 (2011) 3385.
[35] S. Heyraud, P.E.R. Blanchard, S. Liu, Q. Zhou, B.J. Kennedy, H.E.A. Brand, A. Tadich, J.R. Hester, J. Phys. Condens. Matter. 25 (2013) 335401.
[36] J. Sugar, W.D. Brewer, G. Kalkowski, G. Kaindl, E. Paparazzo, Phys. Rev. A 32 (1985) 2242.
[37] P. Vavassori, L. Duò, G. Chiaia, M. Qvarford, I. Lindau, Phys. Rev. B 52 (1995) 16503.
[38] R.F. Egerton, Electron Energy-Loss Spectroscopy in the Electron Microscope, Springer, New York 2011, p. 206.
[39] Calculated using the QUASESIMFP-TPP2M software; 〈http://www.quases.com/products/quases-imfp-tpp2m/〉.
[40] P.P. Dholabhai, J.B. Adams, P.A. Crozier, R. Sharma, J. Chem. Phys. 132 (2010) 094104.